INTERNATIONAL JOURNAL FOR NUMERICAL METHODS IN BIOMEDICAL ENGINEERING
Int. J. Numer. Meth. Biomed. Engng. 2012; **28**:187–204
Published online 19 July 2011 in Wiley Online Library (wileyonlinelibrary.com). DOI: 10.1002/cnm.1453

A localized meshless approach for modeling spatial–temporal calcium dynamics in ventricular myocytes

Guangming Yao and Zeyun Yu*,†

Department of Computer Science, University of Wisconsin-Milwaukee, Milwaukee, WI 53211, U.S.A.

SUMMARY

Spatial–temporal calcium dynamics due to calcium release, buffering and re-uptaking plays a central role in studying excitation–contraction (E–C) coupling in both normal and diseased cardiac myocytes. In this paper, we employ a meshless method, namely, the local radial basis function collocation method (LRBFCM), to model such calcium behaviors by solving a nonlinear system of reaction–diffusion partial differential equations. In particular, a simplified structural unit containing a single transverse tubule (T-tubule) and its surrounding half sarcomeres is investigated using the meshless method. Numerical results are compared with those generated by finite element methods, showing the capability and efficiency of the LRBFCM in modeling calcium dynamics in ventricular myocytes. The single T-tubule model is also extended to the whole-cell scale with T-tubules excluded to demonstrate the scalability of the proposed meshless method in handling very large domains. The experiments have shown that the LRBFCM is suitable to multiscale modeling of calcium dynamics in ventricular myocytes with high accuracy and efficiency. Copyright © 2011 John Wiley & Sons, Ltd.

Received 8 February 2011; Revised 17 April 2011; Accepted 20 April 2011

KEY WORDS: meshless methods; local radial basis function collocation method (LRBFCM); numerical simulation; calcium dynamics; ventricular myocytes

1. INTRODUCTION

Heart failure has been one of the leading causes of human deaths in many countries including the USA. The prevalence of this disease is largely due to our lack of accurate understanding of excitation–contraction (E–C) coupling in cardiomyocytes. In particular, the architecture of uniquely developed membrane organelles in ventricular myocytes, including transverse tubules (T-tubules) and junctional sarcoplasmic reticulum (SR), and the arrangement of associated proteins are known to play a major role in dynamically controlling intracellular calcium levels, which in turn regulate cardiac contraction and other cellular functions [1]. For its central role in E–C coupling, modeling Ca^{2+} release and concentration change has been an active research area and is typically studied in two ways: stochastic approaches that employ Monte Carlo simulation at the nanometer scale [2] and deterministic approaches based on partial differential equations (PDEs) at the micrometer scale [3]. Although stochastic simulation at the nanometer scale provides elementary information on calcium dynamics, cardiac cell contraction is most closely related to the intracellular calcium concentration level $[Ca^{2+}]_i$ [4]. For this reason, our interest in the present paper is to investigate spatial–temporal variations of intracellular calcium concentration at cellular and subcellular levels, where the stochastic behavior of calcium dynamics is insignificant so that deterministic methods utilizing PDEs are more appropriate.

*Correspondence to: Zeyun Yu, Department of Computer Science, University of Wisconsin-Milwaukee, Milwaukee, WI 53211, U.S.A.
†E-mail: yuz@uwm.edu.

A set of PDEs may be numerically solved by such traditional approaches as the finite difference method (FDM) [5], the finite element method (FEM) [6, 7], the finite volume method (FVM) [8], and the boundary element method (BEM) [9, 10]. Despite their great success in the past decades in many branches of science and engineering, these mesh-based methods require meshes or grids as the solution domain. The costs and difficulties in creating quality meshes, however, constitute one of the major bottlenecks in these methods. Therefore, the meshless method that uses only a set of unconnected and arbitrarily placed nodes to discretize a domain has become a popular technique in many fields such as fluid dynamics, solid mechanics, and computational mathematics [11–15]. Detailed discussion on the meshless method and its applications to many complex and large-scale PDE-based problems can be found in [13, 15–19].

The main advantages of the meshless method for solving PDEs lie in its simplicity, applicability to various PDEs, and effectiveness in dealing with nonlinear and high-dimensional problems with complicated geometries [20]. Much as with the FDM or the FEM, it has long been recognized that, with global meshless methods, restriction on the size of the computational stencil is a necessity in order to achieve stability. To avoid ill-conditioned problems and to reduce computational costs involved in solving large-scale problems using global meshless methods, various localized meshless methods have recently been developed [21–23]. One significant development is the local radial basis function collocation method (LRBFCM) developed by Šarler and Vertnik [23]. Previous work has shown LRBFCM's accuracy and efficiency in various complex problems such as convection–diffusion problems with phase-change [24], continuous casting [25], solid–solid phase transformations [26], Navier Stokes equations [27], Darcy flow [28], turbulent flow [29], and so on. The main feature of the LRBFCM is that collocation takes place on overlapping local domains. This drastically reduces the size of the collocation matrix. The price paid, however, is that many small matrices must now be solved. Because the LRBFCM does not experience any significant loss of accuracy in comparison with the global version, it has been applied to many complicated PDE problems, including large-scale industrial applications. It is apparent that localized meshless methods can compete with traditional numerical methods for solving large-scale PDEs. Thanks to the collocation approach, no numerical integration is required in the LRBFCM, which makes it easy for this approach to handle extremely irregular domains by adopting a random node arrangement.

In this paper, we apply the LRBFCM meshless method to solve a set of PDEs that govern calcium dynamics in ventricular myocytes. The rest of the paper is organized as follows. The governing system of PDEs are introduced in Section 2. In Section 3, we briefly describe the operator-splitting method to decouple the PDEs and to separate nonlinear sources and Laplacian operators. The LRBFCM is briefly reviewed in the beginning of Section 4, followed by an extension of the scaling technique in [23] to three-dimensional (3D) cases allowing us to alleviate the difficulty of finding suitable shape parameters. In Section 5, various numerical experiments are conducted and compared with those generated by the FEM in [30] to validate the proposed meshless approach. We draw the conclusion in Section 6.

2. GOVERNING EQUATIONS

The following nonlinear reaction–diffusion equations are modified from [30]:

$$\frac{\partial[\mathrm{Ca}^{2+}]_i}{\partial t} = D_{\mathrm{Ca}}\nabla^2[\mathrm{Ca}^{2+}]_i - \sum_{m=1}^{3} R_{Bm} - R_{Bs}, \quad \text{in } \Omega, \tag{1}$$

$$\frac{\partial[\mathrm{Ca}B_m]}{\partial t} = D_{\mathrm{Ca}B_m}\nabla^2[\mathrm{Ca}B_m] + R_{Bm}, \quad \text{in } \Omega, \quad m = 1, 2, 3, \tag{2}$$

$$\frac{\partial[\mathrm{Ca}B_s]}{\partial t} = R_{B_s}, \quad \text{in } \Omega, \tag{3}$$

$$\frac{\partial[\mathrm{Ca}^{2+}]_i}{\partial t} = D_{\mathrm{Ca}}\nabla^2[\mathrm{Ca}^{2+}]_i + J_{\mathrm{Caflux}}, \quad \text{on } \partial\Omega, \tag{4}$$

DOI: 10.1002/cnm

with initial conditions:

$$[Ca^{2+}]_i = 0.10\ \mu M, \quad [CaB_1] = 11.92\ \mu M, \quad [CaB_2] = 0.97\ \mu M,$$
$$[CaB_3] = 0.13\ \mu M, \quad [CaB_s] = 6.36\ \mu M,$$

and reflective boundary condition, where $\Omega \subset \mathbb{R}^3$, and $\partial\Omega$ is the cell surface and T-tubule membrane. The reactions between calcium ions and buffers are given by the following:

$$R_{Bm} = k_+^m ([B_m] - [CaB_m])\,[Ca^{2+}]_i - k_-^m [CaB_m], \quad m = 1, 2, 3, \tag{5}$$
$$R_{Bs} = k_+^m ([B_s] - [CaB_s])\,[Ca^{2+}]_i - k_-^m [CaB_s]. \tag{6}$$

In our model, three types of mobile Ca^{2+} buffers (Fluo-3, ATP, and calmodulin, denoted by B_m, $m = 1, 2, 3$) and one type of stationary Ca^{2+} buffers (troponin, denoted by B_s) are considered. Their concentrations are denoted respectively by the following: $[Ca^{2+}]_i$; $[CaB_m], m = 1, 2, 3$; $[CaB_s]$. At the resting (initial) state, all the buffers are distributed uniformly throughout the cytosol but not on the cell membrane. The resting concentrations of mobile and stationary buffers satisfy equilibrium conditions (i.e., $R_{Bm} = R_{Bs} = 0$) [31]. The initial concentrations of buffers are calculated in equilibrium with the resting Ca^{2+} concentration, 0.1 μM. The total Ca^{2+} flux, J_{Caflux}, on the surface membrane is defined as in [30], where Ca^{2+} influx/efflux through L-type calcium channels (LCCs), sodium–calcium exchangers (NCXs), Ca^{2+} pumps and background leaks are included. The total Ca^{2+} flux (J_{Caflux}) throughout the cell surface membrane and the surface of T-tubules is as follows [1]:

$$J_{Caflux} = J_{Ca} + J_{NCX} - J_{pCa} + J_{Cab}, \tag{7}$$

where J_{Ca} is total LCC Ca^{2+} influx, J_{NCX} is total NCX Ca^{2+} efflux, J_{pCa} is total Ca^{2+} pump efflux, and J_{Cab} is the total background Ca^{2+} leak influx. We use the following expressions from [32, 33] to describe the current densities:

$$I_{Ca} = \begin{cases} 0.05978\,t, & t \in (0, 4\ \text{ms}], \\ 0.02327 + 0.11931\left[e^{-t/55.900350} + e^{-t/55.89166}\right], & t \in (4\ \text{ms}, 70\ \text{ms}], \\ 0, & t \in (70\ \text{ms}, \infty), \end{cases} \tag{8}$$

$$I_{NCX} = g_{NCX} \frac{e^{\eta V F/R\,T}[Na^+]_i^3[Ca^{2+}]_e - e^{(\eta-1)V F/R\,T}[Na^+]_e^3[Ca^{2+}]_i}{\left(k_{m,Na}^3 + [Na^+]_e^3\right)\left(k_{m,Ca} + [Ca^{2+}]_e\right)\left(1 + k_{sat}e^{(\eta-1)V F/R\,T}\right)}, \tag{9}$$

$$I_{pCa} = \frac{g_{pCa}[Ca^{2+}]_i}{[Ca^{2+}]_i + k_{m,pCa}}, \tag{10}$$

$$I_{Cab} = g_{Cab}\left[\frac{R\,T}{2F}\ln\left(\frac{[Ca^{2+}]_e}{[Ca^{2+}]_i}\right) - V\right], \tag{11}$$

where I_{Ca} is the LCC current density, I_{NCX} is the Na^+/Ca^+ exchanger, I_{pCa} is the membrane $[Ca^{2+}]_i$ pump, and I_{Cab} represents the leak current density. The physical constants and parameters are summarized in Table I.

To calculate the total Ca^{2+} flux, J_{Caflux}, each of the current densities, I_i ($\mu M\,ms^{-1}$), is converted to Ca^{2+} flux, J_i ($\mu M\,ms^{-1}$), by using the suggested experimental capacitance to rendered volume ratio, ($C_m/V_{cell} = 8.8\ pF\,pL^{-1}$) [36]:

$$J_i = \beta\frac{V_{mc}}{S_i}\left(\frac{1}{2F}\frac{C_m}{V_{cell}}\right)I_i, \tag{12}$$

DOI: 10.1002/cnm

Table I. The parameters used in the paper.

Name	Symbol	Value	Ref.
Physical constants			
Faraday constant	F	96.5 C mmol^{-1}	Constant
Temperature	T	295 K	Constant
Universal gas constant	R	8.314 J mol^{-1} K^{-1}	Constant
T-tubule depth	h	6.8 μm	[34]
Ca^{2+} and buffer concentrations			
Extracellular Ca^{2+} concentration	$[Ca^{2+}]_i$	1000 μM	[4]
Resting Ca^{2+} concentration	$[Ca^{2+}]_{i\,0}$	0.1 μM	[4]
Fluo-3 concentration	[Fluo]	100 μM	[35]
Free ATP concentration	[ATP]	260 μM	[35]
Troponin concentration	[TN]	70 μM	[35]
Calmodulin concentration	[Cal]	24 μM	[35]
Diffusion coefficients			
Diffusion coefficient for Ca^{2+}	D_{Ca}	0.39 μm^2 ms^{-1}	[35]
Diffusion coefficient for CaFluo	$D_{\mathrm{Ca\,Fluo}}$	0.1 μm^2 ms^{-1}	[35]
Diffusion coefficient for CaATP	$D_{\mathrm{Ca\,ATP}}$	0.168 μm^2 ms^{-1}	[35]
Diffusion coefficient for CaCal	$D_{\mathrm{Ca\,Cal}}$	0.025 μm^2 ms^{-1}	[35]
Rate coefficients			
Ca^{2+} on-rate constant for TN	k_+^{CaTN}	0.04 μM^{-1} ms^{-1}	[35]
Ca^{2+} off-rate constant for TN	k_-^{CaTN}	0.04 μM^{-1} ms^{-1}	[35]
Ca^{2+} on-rate constant for ATP	k_+^{CaATP}	0.225 μM^{-1} ms^{-1}	[35]
Ca^{2+} off-rate constant for ATP	k_-^{CaATP}	45 μM^{-1} ms^{-1}	[35]
Ca^{2+} on-rate constant for Fluo-3	k_+^{CaFluo}	0.23 μM^{-1} ms^{-1}	[35]
Ca^{2+} off-rate constant for Fluo-3	k_-^{CaFluo}	0.17 μM^{-1} ms^{-1}	[35]
Ca^{2+} on-rate constant for Calmodulin	k_+^{CaCal}	0.125 μM^{-1} ms^{-1}	[35]
Ca^{2+} off-rate constant for Calmodulin	k_+^{CaCal}	0.2975 μM^{-1} ms^{-1}	[35]
Membrane Ca^{2+} flux parameters			
Na^+/Ca^+ exchange current			
Extracellular Na^+ concentration	$[Na_e^+]$	140 mM	[4]
Resting Na^+ concentration	$[Na_i^+]$	10 mM	[4]
Pump rate of NCX	g_{NCX}	38.5 μM ms^{-1}	[33]
Voltage dependence of NCX control	η	0.35	[33]
Na^+ half saturation of NCX	$k_{m,\mathrm{Na}}$	87.5 mM	[33]
Ca^{2+} half saturation of NCX	$k_{m,\mathrm{Ca}}$	1380 μM	[33]
Low potential saturation factor of NCX	k_{sat}	0.1	[33]
Membrane Ca^{2+} ATPase			
Maximum Ca^{2+} pump rate	g_{pCa}	0.0035 μM ms^{-1}	[33]
Half saturation of Ca^{2+} pump	$k_{m,\mathrm{pCa}}$	0.5 μM	[33]
Membrane Ca^{2+} leak			
Conductance of sarcolemmal Ca^{2+} leak	g_{Cab}	1.65E−5 μM mV^{-1} ms^{-1}	Estimated

ATP, adenosine triphospate; NCX, sodium–calcium exchangers; T-tubule, transverse tubule.

with i = Ca, NCX, pCa, or Cab. Note that S_i is the total area of surface membrane and T-tubule membrane where calcium-related channels reside and V_{mc} is the volume of the model being considered. β is a model-dependent scaling parameter. The voltage-clamp protocol is assumed to hold potential −50 mV with an electric pulse of 10 mV for 70 ms, that is,

$$V = \begin{cases} 10\ \mathrm{mV}, & t \in (0, 70\ \mathrm{ms}], \\ -50\ \mathrm{mV}, & t \in (70\ \mathrm{ms}, \infty). \end{cases} \tag{13}$$

In the present work, two geometric models are considered:

I. According to [34, 37], ventricular myocytes may be simplified to repeated structural units consisting of a single T-tubule and its surrounding half sarcomeres. The surrounding half

DOI: 10.1002/cnm

sarcomeres are modeled as a cube-shaped box with a dimension of length 7 μm, width 2 μm, and depth 2 μm, enclosing a T-tubule of 6.8 μm × 0.2 μm × 0.2 μm. The T-tubule is assumed to be a tiny cube located vertically in the center of the domain, as shown on the left of Figure 1. This simplified geometric model had been studied in [30], where the FEM was utilized to find the numerical solutions of the equations. The same geometry is considered in our work so that we can validate our meshless numerical approach. In addition, we also experimented a special case where the T-tubule is 'reduced' into a single line (with zero thickness).

II. We shall also consider a simplified whole-cell model, as shown on the right of Figure 1. The cell surface is described by the following parametric equation:

$$r(\theta,\phi) = 35\,\mathrm{R}(\theta)\cos(\theta)\mathbf{i} + 10\,\mathrm{R}(\theta)\sin(\theta)\cos(\phi)\mathbf{j} + 10\,\mathrm{R}(\theta)\sin(\theta)\sin(\phi)\mathbf{k}, \tag{14}$$

where $\theta \in [0,\pi), \phi \in [0,2\pi)$, and $\mathrm{R}(\theta) = \sqrt{\cos(2\,\theta) + \sqrt{4-\sin^2(2\,\theta)}}$. With this model, we aim to predict spatial–temporal calcium concentrations in the absence of T-tubule systems. The question of interest is to predict a high gradient near the cell membrane and a more uniform calcium distribution in the cell interior.

To solve the system of equations in Equations (1)–(4) with meshless techniques, we use an explicit time-stepping method in time dimension and the LRBFCM [23] in space dimension. The details of the algorithm are given in the following sections.

3. OPERATOR-SPLITTING METHOD

Rewrite the diffusion–reaction equations in Equations (1)–(4) as

$$\frac{\partial u(\mathbf{x},t)}{\partial t} = \mu\nabla^2 u(\mathbf{x},t) + \mathrm{f}(u(\mathbf{x},t)), \tag{15}$$

where $\mathbf{x} = (x,y,z) \in \Omega$ and u stands for the concentration of calcium and buffers, that is, $[\mathrm{Ca}^{2+}]_i, [\mathrm{Ca}B_m]$, or $[\mathrm{Ca}B_s]$. The diffusion coefficients D_{Ca} and $D_{\mathrm{Ca}B_m}$ are denoted by μ. The

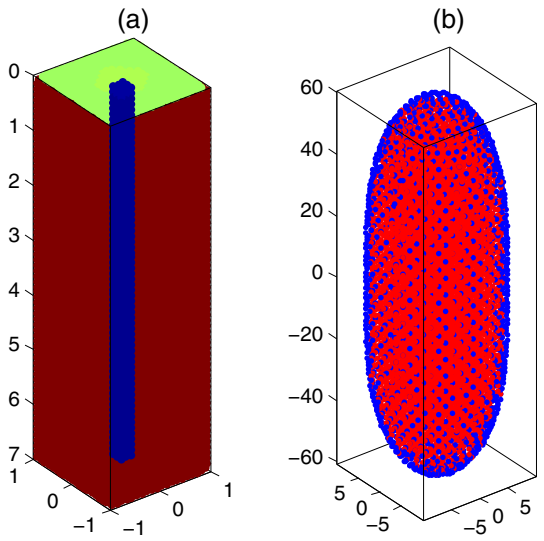

Figure 1. Two computational models considered (unit: μm). Left: single T-tubule model with the T-tubule (blue), the surrounding half sarcomere (red), and the external cell membrane (green). A total of 24 297 interior points and 6510 boundary points are distributed in the domain and used in the meshless method. Right: the whole-cell model with the cell membrane (blue) and the cell cytosol (red). Note that T-tubules are excluded from the whole-cell model and the blue dots (a total of 7065) shown are the actual nodes used by the meshless method.

DOI: 10.1002/cnm

reaction and total Ca^{2+} flux are combined as a source function $f(u(\mathbf{x},t))$. The time domain is uniformly discretized with an interval Δt. For simplicity, we only consider below two consecutive time steps, t_s and t_{s+1}, referred to as 'previous' and 'current' time steps, respectively. For sufficiently small Δt ($t_{s+1} = t_s + \Delta t$), we have

$$\frac{\partial u(\mathbf{x},t)}{\partial t} = \frac{u(\mathbf{x},t_{s+1}) - u(\mathbf{x},t_s)}{\Delta t} + \mathcal{O}(\Delta t). \tag{16}$$

Then, Equation (15) can be approximated by

$$\frac{u(\mathbf{x},t_{s+1}) - u(\mathbf{x},t_s)}{\Delta t} = \mu\nabla^2 u(\mathbf{x},t) + f(u(\mathbf{x},t)), \quad t \in (t_s, t_{s+1}]. \tag{17}$$

To decompose the elliptic differential operator and the nonlinear forcing term into simpler subproblems and thus solve them individually using suitable numerical algorithms, we use the first-order operator-splitting method [38], yielding the following two subproblems:

$$\frac{u(\mathbf{x},t_{s+1/2}) - u(\mathbf{x},t_s)}{\Delta t} = f(u(\mathbf{x},t_s)), \tag{18}$$

and

$$\frac{u(\mathbf{x},t_{s+1}) - u(\mathbf{x},t_{s+1/2})}{\Delta t} = \mu\nabla^2 u(\mathbf{x},t_{s+1/2}). \tag{19}$$

Rearranging the above equations, we have

$$u(\mathbf{x},t_{s+1/2}) = u(\mathbf{x},t_s) + \Delta t f(u(\mathbf{x},t_s)), \tag{20}$$

and

$$u(\mathbf{x},t_{s+1}) = u(\mathbf{x},t_{s+1/2}) + \mu\Delta t\nabla^2 u(\mathbf{x},t_{s+1/2}). \tag{21}$$

Substituting Equation (20) into Equation (21), we have

$$u(\mathbf{x},t_{s+1}) = u(\mathbf{x},t_s) + \Delta t f(u(\mathbf{x},t_s) + \mu\Delta t\nabla^2 u(\mathbf{x},t_{s+1/2}), \tag{22}$$

where the values $u(\mathbf{x},t_{s+1/2})$ are calculated from Equation (20) and the Laplacian term, $\nabla^2 u(\mathbf{x},t_{s+1/2})$, is approximated by using the meshless method, as detailed in the next section.

4. SPACE DISCRETIZATION: LOCAL RADIAL BASIS FUNCTION COLLOCATION METHOD

In this section, we introduce the LRBFCM [23] to approximate $\nabla^2 u(\mathbf{x},t_{s+1/2})$ in Equation (22). Interested readers may refer to [13, 15] for more details on the meshless method. The main idea of the LRBFCM is the collocation on overlapping local domains, which drastically reduces the collocation matrix size at the expense of solving many small matrices. The sizes of matrices depend on the number of nodes included in the local domain of each node.

As the name implies, radial basis functions (RBFs) are utilized in the LRBFCM, as in many other meshless methods. Therefore, this section begins by introducing some basic features of RBFs in order to develop properties necessary for use with the LRBFCM.

Definition 1
Let $\mathbf{R}^d$ be a d-dimensional Euclidean space. Let $\mathbf{c} \in \mathbf{R}^d$ and $\Phi : \mathbf{R}^d \to \mathbf{R}$ be an invariant function whose value at any point $\mathbf{x} \in \mathbf{R}^d$ depends only on the distance from the fixed point $\mathbf{c}$ and can be written as

$$\Phi(\|\mathbf{x} - \mathbf{c}\|). \tag{23}$$

Then, the function Φ is an RBF, where $\mathbf{c}$ is the center of Φ.

DOI: 10.1002/cnm

The variable $r = \|\mathbf{x} - \mathbf{c}\|$ is often used in RBFs and thus is adopted in this study. Micchelli [39] proved that the distance matrix generated by distinct points using the Euclidean norm is invertible for several types of RBFs. Thus, this paper utilizes only the Euclidean norm. Several commonly used RBFs are multiquadrics (MQ), inverse multiquadrics (IMQ), Gaussian, thin-plate splines, polyharmonic splines, and so on. MQ RBF has been proved to have a high-order rate of convergence. Thus, in this paper, we use MQ, that is,

$$\Phi(r) = \sqrt{r^2 + c^2}, \tag{24}$$

where $c > 0$ is called a shape parameter.

In the LRBFCM, the value of $\nabla^2 u(\mathbf{x}, t_{s+1/2})$ at each node $\mathbf{x}_i, i = 1, 2, \ldots, N$, is approximated by the values at the neighbors of $\mathbf{x}_i$. The local domain, Ω_i, associated with $\mathbf{x}_i$ can be created using the n nearest neighbors to $\mathbf{x}_i$ including itself, that is, $\{\mathbf{x}_k^{[i]}\}_{k=1}^n \subset \Omega_i$. In this paper, the number of points in each local domain is fixed as $n = 7$. Figure 2 shows the seven-node local domain, Ω_i, including the center node, $\mathbf{x}_i$, and its six neighbors. Note that our model includes net fluxes through cell surface and T-tubule membrane, so the diffusion on $\partial\Omega$ does not include the diffusion between boundary points. Thus, the neighborhood of a boundary point contains only interior points. By Equation (20), the concentration, $u(\mathbf{x}_i, t_{s+1/2})$, is known at every node $\mathbf{x}_i$. To approximate $\nabla^2 u(\mathbf{x}_i, t_{s+1/2})$, we create a local domain Ω_i, and interpolate $u(\mathbf{x}, t_{s+1/2})$ on Ω_i using RBFs $\Phi(r)$ with different centers $\mathbf{x}_k^{[i]}, k = 1, 2, \ldots, n$. Thus, we have

$$u(\mathbf{x}_j^{[i]}, t_{s+1/2}) = \sum_{k=1}^{n} \Phi(\|\mathbf{x}_j^{[i]} - \mathbf{x}_k^{[i]}\|)\alpha_k^{[i]}, \quad j = 1, 2, \ldots, n. \tag{25}$$

This is an n by n system of linear equations:

$$\begin{bmatrix} u\left(\mathbf{x}_1^{[i]}, t_{s+1/2}\right) \\ u\left(\mathbf{x}_2^{[i]}, t_{s+1/2}\right) \\ \vdots \\ u\left(\mathbf{x}_n^{[i]}, t_{s+1/2}\right) \end{bmatrix} = \begin{bmatrix} \Phi\left(\|\mathbf{x}_1^{[i]} - \mathbf{x}_1^{[i]}\|\right) & \Phi\left(\|\mathbf{x}_1^{[i]} - \mathbf{x}_2^{[i]}\|\right) & \ldots & \Phi\left(\|\mathbf{x}_1^{[i]} - \mathbf{x}_n^{[i]}\|\right) \\ \Phi\left(\|\mathbf{x}_2^{[i]} - \mathbf{x}_1^{[i]}\|\right) & \Phi\left(\|\mathbf{x}_2^{[i]} - \mathbf{x}_2^{[i]}\|\right) & \ldots & \Phi\left(\|\mathbf{x}_2^{[i]} - \mathbf{x}_n^{[i]}\|\right) \\ \vdots & \vdots & \vdots & \vdots \\ \Phi\left(\|\mathbf{x}_n^{[i]} - \mathbf{x}_1^{[i]}\|\right) & \Phi\left(\|\mathbf{x}_n^{[i]} - \mathbf{x}_2^{[i]}\|\right) & \ldots & \Phi\left(\|\mathbf{x}_n^{[i]} - \mathbf{x}_n^{[i]}\|\right) \end{bmatrix} \begin{bmatrix} \alpha^{[i]}{}_1 \\ \alpha^{[i]}{}_2 \\ \vdots \\ \alpha^{[i]}{}_n \end{bmatrix}. \tag{26}$$

It can be written in a matrix notation as

$$\mathbf{u}^{[i]} = \mathbf{P}_{nn}\boldsymbol{\alpha}^{[i]}, \tag{27}$$

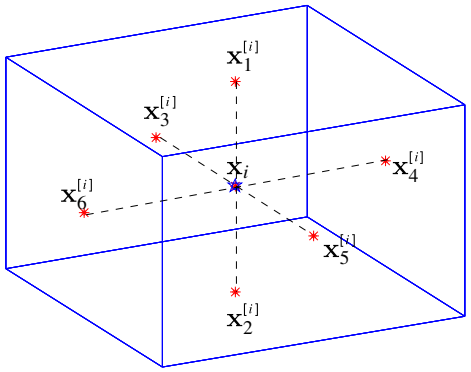

Figure 2. Schematic diagram showing the seven-node local domain of the i-th node, $\mathbf{x}_i$.

DOI: 10.1002/cnm

where $\boldsymbol{\alpha}^{[i]} = [\alpha_1^{[i]}, \alpha_2^{[i]}, \ldots, \alpha_n^{[i]}]^{\mathrm{T}}$ and $P_{jk} = \Phi(\|\mathbf{x}_j^{[i]} - \mathbf{x}_k^{[i]}\|)$ being the entry element of the matrix of $\mathbf{P}_{nn}$ at the jth row and the kth column, and

$$\mathbf{u}^{[i]} = [u(\mathbf{x}_1^{[i]}, t_{s+1/2}), u(\mathbf{x}_2^{[i]}, t_{s+1/2}), \ldots, u(\mathbf{x}_n^{[i]}, t_{s+1/2})]^{\mathrm{T}}. \tag{28}$$

The unknown coefficients, $\boldsymbol{\alpha}^{[i]}$, can be obtained by inverting the matrix in Equation (27), that is,

$$\alpha_k^{[i]} = \sum_{j=1}^{n} P_{kj}^{-1} u(\mathbf{x}_j^{[i]}, t_{s+1/2}), \quad k = 1, 2, \ldots, n. \tag{29}$$

Note that P_{kj}^{-1} is the kth row and jth column of inverse matrix, $\mathbf{P}_{nn}^{-1}$. From Equations (24) and (25), we have

$$\nabla^2 u(\mathbf{x}_i, t_{s+1/2}) = \sum_{k=1}^{n} \nabla^2 \Phi(\|\mathbf{x}_i - \mathbf{x}_k^{[i]}\|) \alpha_k^{[i]}, \tag{30}$$

where by direct differentiation,

$$\phi(r) := \nabla^2 \Phi(r) = \frac{2r^2 + 3c^2}{(r^2 + c^2)^{3/2}}.$$

As a result,

$$\nabla^2 u(\mathbf{x}_i, t_{s+1/2}) = \sum_{k=1}^{n} \phi(\|\mathbf{x}_i - \mathbf{x}_k^{[i]}\|) \left(\sum_{j=1}^{n} P_{jk}^{-1} u(\mathbf{x}_j^{[i]}, t_{s+1/2}) \right). \tag{31}$$

Let

$$\boldsymbol{\Lambda}\,(\mathbf{x}_i) = [\Lambda_1(\mathbf{x}_i), \Lambda_2(\mathbf{x}_i), \ldots, \Lambda_n(\mathbf{x}_i)] \tag{32}$$

where

$$\Lambda_j\,(\mathbf{x}_i) = \sum_{k=1}^{n} \phi(\|\mathbf{x}_i - \mathbf{x}_k^{[i]}\|) P_{jk}^{-1}. \tag{33}$$

Rearranging Equation (31), we have

$$\nabla^2 u(\mathbf{x}_i, t_{s+1/2}) = \sum_{j=1}^{n} \Lambda_j(\mathbf{x}_i) u(\mathbf{x}_j^{[i]}, t_{s+1/2}). \tag{34}$$

This gives an approximation of $u(\mathbf{x}_i, t_{s+1})$ using Equation (22):

$$u(\mathbf{x}_i, t_{s+1}) = u(\mathbf{x}, t_s) + \Delta t \mathrm{f}(u(\mathbf{x}, t_s) + \mu \Delta t \sum_{j=1}^{n} \Lambda_j(\mathbf{x}_i) u(\mathbf{x}_j^{[i]}, t_{s+1/2}). \tag{35}$$

The RBF shape parameter in MQ plays a major role in improving the accuracy of numerical solutions [40, 41]. In general, the optimal shape parameter depends on the densities, distributions, and function values at the nodes. However, it is very difficult to assign different free parameters for each local domain. Thus, choosing shape parameters has been an active topic in approximation theory. It has been showed that the scaling technique allows a large range of acceptable shape parameters, while greater shape parameters perform more accurately than smaller ones [23]. We extend the scaling technique in [23] to 3D case. It can be done in each of the x, y, and z directions in the local domain. Let $\mathbf{x}_j^{[i]} = (x_j^{[i]}, y_j^{[i]}, z_j^{[i]})$, $j = 1, 2, \ldots, n$. We define

$$x_m = \max_{1 \leq j,k \leq n} \|x_j^{[i]} - x_k^{[i]}\|, \; y_m = \max_{1 \leq j,k \leq n} \|y_j^{[i]} - y_k^{[i]}\|, \; z_m = \max_{1 \leq j,k \leq n} \|z_j^{[i]} - z_k^{[i]}\|, \tag{36}$$

DOI: 10.1002/cnm

The normalized MQ RBF can then be written as

$$\Phi(r) = \sqrt{\left(\frac{x-x_c}{x_m}\right)^2 + \left(\frac{y-y_c}{y_m}\right)^2 + \left(\frac{z-z_c}{z_m}\right)^2 + c^2}. \tag{37}$$

By simple differentiations, we have

$$\frac{\partial^2 \Phi(r)}{\partial x^2} = \frac{(y-y_c)^2/y_m^2 + (z-z_c)^2/z_m^2 + c^2}{x_m^2 (r^2+c^2)^{3/2}}, \tag{38}$$

$$\frac{\partial^2 \Phi(r)}{\partial y^2} = \frac{(x-x_c)^2/x_m^2 + (z-z_c)^2/z_m^2 + c^2}{y_m^2 (r^2+c^2)^{3/2}}, \tag{39}$$

$$\frac{\partial^2 \Phi(r)}{\partial z^2} = \frac{(x-x_c)^2/x_m^2 + (y-y_c)^2/y_m^2 + c^2}{z_m^2 (r^2+c^2)^{3/2}}, \tag{40}$$

where $r = \sqrt{(x-x_c)^2/x_m^2 + (y-y_c)^2/y_m^2 + (z-z_c)^2/z_m^2}$. Thus,

$$\begin{aligned}\nabla^2 \Phi(r) &= \frac{\partial^2 \Phi(r)}{\partial x^2} + \frac{\partial^2 \Phi(r)}{\partial y^2} + \frac{\partial^2 \Phi(r)}{\partial z^2} \\ &= \frac{(y-y_c)^2/y_m^2 + (z-z_c)^2/z_m^2 + c^2}{x_m^2 (r^2+c^2)^{3/2}} + \frac{(x-x_c)^2/x_m^2 + (z-z_c)^2/z_m^2 + c^2}{y_m^2 (r^2+c^2)^{3/2}} \\ &\quad + \frac{(x-x_c)^2/x_m^2 + (y-y_c)^2/y_m^2 + c^2}{z_m^2 (r^2+c^2)^{3/2}}.\end{aligned} \tag{41}$$

In particular, when $x_m = y_m = z_m$ (denoted by r_m), the MQ RBF is scaled as

$$\Phi(r) = \frac{1}{r_m}\sqrt{r^2 + r_m^2 c^2} \quad \text{and} \quad \nabla^2 \Phi(r) = \frac{1}{r_m}\frac{2r^2 + 3r_m^2 c^2}{(r^2 + r_m^2 c^2)^{3/2}}, \tag{42}$$

where $r = \sqrt{(x-x_c)^2 + (y-y_c)^2 + (z-z_c)^2}$.

After re-scaling the interpolating RBFs, a relatively large shape parameter c can be used even for extremely small grid distances. In the rest of this paper, $c = 300$ is used.

5. SOLUTION PROCEDURE

In this section, the solution procedure to approximate spatial–temporal calcium concentrations is presented. The coupled system described in Equations (1)–(4) is solved by the following steps:

1. Set the initial conditions and boundary conditions at the domain nodes.
2. Search the n nearest neighbors of every node.
3. Calculate the unique vector, $\mathbf{\Lambda}(\mathbf{x}_i)$, defined in Equation (32), for each node $\mathbf{x}_i$.
4. Solve the diffusion–reaction equations for each time step (e.g., from t_s to t_{s+1}).
   - 4.1 Calculate J_{Caflux}, R_{Bm}, and R_{Bs}, $m = 1, 2, 3$.
   - 4.2 Approximate the concentration of the stationary buffer, $[\text{Ca}B_s]$, by Equation (20). In this case, t_{s+1} instead of $t_{s+1/2}$ is used as there is no diffusion term in the stationary buffer.
   - 4.3 Use the initial conditions and Equation (20) to approximate $[\text{Ca}B_m]$, $[\text{Ca}^{2+}]_i$ at $t_{s+1/2}$, $m = 1, 2, 3$.
   - 4.4 Use Equation (34) to approximate the Laplacian operators $\nabla^2[\text{Ca}B_m]$, $\nabla^2[\text{Ca}^{2+}]_i$ at $t_{s+1/2}$.
   - 4.5 Use Equation (21) to approximate concentrations $[\text{Ca}B_m]$, $[\text{Ca}^{2+}]_i$ at t_{s+1}.
   - 4.6 Update $[\text{Ca}B_m]$, $[\text{Ca}^{2+}]_i$, and $[\text{Ca}B_s]$ with the concentrations at t_{s+1}.
5. Repeat Step 4.

In Step 2 of the solution procedure, we must find the local domains Ω_i for each node $\mathbf{x}_i, i = 1, \ldots, N$, such that Ω_i includes the n closest points to $\mathbf{x}_i$. For a large number of collocation points

DOI: 10.1002/cnm

or a high-dimensional space, the time consumption can be very high if a brute-force searching algorithm is used. There are a number of established methods of finding the nearest neighbors of a given point [42–46]. In our work, the k-dimensional tree (or kd-tree for short) data structure is used for its high efficiency [42,43]. In Step 3, there are N small matrices with a dimension of $n \times n$ that need to be inverted. The positive definiteness of MQ RBFs guarantees the existence of the inverse matrices. Because the weights depend only on the locations of the neighbors and are time-independent, the weights can be precomputed and stored in the vector $\mathbf{\Lambda}(\mathbf{x}_i)$.

The most time-consuming parts of the procedure are Steps 4 and 5 because the solutions of the diffusion–reaction equations have to be iteratively updated. To find the steady-state solution to the system of PDEs, the following convergence criterion may be used:

$$\max |u(\mathbf{x}, t_{s+1}) - u(\mathbf{x}, t_s)| \leqslant \epsilon, \tag{43}$$

where ϵ is chosen as the steady-state convergence margin. However, to compare our work with existing results in [30], all the simulations in this paper were conducted for a fixed time period $t \in [0, 400 \text{ ms}]$. Thus, the computational cost will depend on the time-step size. In explicit time-stepping methods, a small sampling distance in space generally implies the need for a small time step, which apparently results in slow convergence. However, large time steps often lead to diverging or oscillating numerical results. A good choice of time-step size can improve the rate of convergence and the stability as well. On the other hand, an explicit time discretization form is only conditionally stable and the stability analysis for diffusion equations yields the following Courant–Friedrichs–Lewy condition [47]:

$$\frac{\mu \Delta t}{h^2} \leqslant \frac{1}{2}, \tag{44}$$

where μ is the diffusion coefficients of calcium and mobile buffers in the present work, Δt is the time-step size, and h is the grid distance. The aforementioned requirement is equivalent to

$$\Delta t \leqslant h^2/2\mu. \tag{45}$$

In our explicit time-stepping strategy, the minimum grid distance $h = 0.1$ μm has been used. The diffusion coefficients are fixed as shown in Table I. Thus, the time-step size approximately satisfies:

$$\Delta t \leqslant 0.01 \text{ ms}. \tag{46}$$

We had chosen the time-step size Δt as 0.004 ms, that is, 4 μs. This is much smaller than 4 ms as in the FEM in [30]. Although it is necessary to have a small time-step size to ensure a stable solution, the meshless method still significantly outperforms the FEM in computational efficiency. As reported in [30], with FEM, it took approximately 18 min to simulate 400 ms of one Ca^{2+} cycle on a cluster of 10 Intel Xeon-based processors with the time step of 4 ms. By contrast, our meshless scheme only took about 5 min to simulate the same time course on a single processor of the same type, despite a much smaller time-step size being used.

6. NUMERICAL RESULTS

In this section, we present the numerical results on two different models using the LRBFCM described earlier.

6.1. Case 1: a single T-tubule model

We first consider the single T-tubule model as shown on the left of Figure 1, where the overall shape is a cube of 7 μm × 2 μm × 2 μm and the T-tubule is vertically placed in the center as a tiny cube of 6.8 μm × 0.2 μm × 0.2 μm. A very similar model has been used in [30] except that the T-tubule in our work is modeled as a cube-shaped box instead of a cylinder. The geometries of the model are derived from earlier studies that T-tubules with diameters ranging from 200–300 nm are mostly found at intervals of about 2 μm near the Z-disks of ventricular myocytes [34]. As in [30], the LCC

DOI: 10.1002/cnm

current density is uniformly distributed on the cell surface and the surface of the T-tubule. The NCX current density is assumed to be three times higher on T-tubular membrane than the cell surface and Ca^{2+} pumps are located only on the cell surface. The surface areas and volumes are listed in Table II.

The conversions from current densities to total Ca^{2+} flux are as follows:

$$J_{\mathrm{Ca}} = \beta \frac{V_{\mathrm{mc}}}{S_{\mathrm{mc}}} \left(\frac{1}{2\mathrm{F}} \frac{C_m}{V_{\mathrm{cell}}} \right) I_{\mathrm{Ca}}, \quad J_{\mathrm{Cab}} = \beta \frac{V_{\mathrm{mc}}}{S_{\mathrm{mc}}} \left(\frac{1}{2\mathrm{F}} \frac{C_m}{V_{\mathrm{cell}}} \right) I_{\mathrm{Cab}}, \tag{47}$$

$$J_{\mathrm{NCX}} = \begin{cases} \dfrac{3\beta V_{\mathrm{mc}}}{3S_{\mathrm{mt}} + S_{\mathrm{ms}}} \left(\dfrac{1}{2\mathrm{F}} \dfrac{C_m}{V_{\mathrm{cell}}} \right) I_{\mathrm{NCX}}, & \text{on T-tubule} \\ \dfrac{\beta V_{\mathrm{mc}}}{3S_{\mathrm{mt}} + S_{\mathrm{ms}}} \left(\dfrac{1}{2\mathrm{F}} \dfrac{C_m}{V_{\mathrm{cell}}} \right) I_{\mathrm{NCX}}, & \text{on cell membrane,} \end{cases} \tag{48}$$

$$J_{\mathrm{pCa}} = \begin{cases} 0, & \text{on T-tubule} \\ \beta \dfrac{V_{\mathrm{mc}}}{S_{\mathrm{ms}}} \left(\dfrac{1}{2\mathrm{F}} \dfrac{C_m}{V_{\mathrm{cell}}} \right) I_{\mathrm{pCa}}, & \text{on cell membrane.} \end{cases} \tag{49}$$

As suggested in [36], the ratio of cell capacitance to volume, C_m / V_{cell}, is assumed to be 8.8 pF pL^{-1}. The scaling parameter β is chosen as 219.25, and a uniformly distributed grid with a sampling distance of 0.1 μm is adopted.

The results in Figure 3 are in agreement with [30], where the Ca^{2+} signals in rat ventricular myocytes are calculated in the presence of 100 μM Fluo-3 and pharmacological blockade of the SR. The global and local Ca^{2+} transients reached the peaks at about 68 ms when the LCC current is completely blocked. Figure 3(a)–(b) shows the voltage-clamp protocol and the whole-cell L-type Ca^{2+} current used in Case 1. Figure 3(c)–(e) shows the averaged current densities of Na^+/Ca^+ exchangers, Ca^{2+} pumps and Ca^{2+} leaks, assuming uniform distribution of Ca^{2+} inside the model. The average current densities are also predicted by using the local Ca^{2+} concentrations near the calcium channels (see Figure 4(a)–(c)) and appear significantly different from Figure 3(c)–(f). Figure 3(f) shows the averaged Ca^{2+} concentration over time. The results shown in Figure 3 are very similar to those in [30]. The only difference is that Ca^{2+} leak is slightly smaller in our case because of the different model-dependent parameter β that is used. The consequence is that the Ca^{2+} concentration is still decreasing even after the Ca^{2+} peak at 68 ms (see Figure 3(f)).

To describe better the predicted Ca^{2+} transients in the model, three scanned lines are chosen at 200, 400, and 700 nm away from the surface of the T-tubule. Also, we select three feature spots along each scanned line at 0.5, 3.6, and 7.0 μm away from the cell surface, see Figure 3(g)–(m), respectively. The model is able to predicate global and local Ca^{2+} transient peaks after approximately 68 ms. The local Ca^{2+} transients near the surface of the T-tubule are slightly different from the other two scanned lines (see Figure 3(g) and (j)) because the scanned line is so close to the T-tubular surface that the total Ca^{2+} flux significantly affects the Ca^{2+} concentration.

The time course concentrations of the mobile and stationary buffers are shown in Figure 4(d)–(g). In the presence of LCC current densities, the concentrations of all buffers increase. The buffers become stable only after the Ca^{2+} concentration change becomes stable. The 3D Ca^{2+} concentrations at 68 and 300 ms are shown in Figure 4(h) and (i), corresponding to the Ca^{2+} peak and stable

Table II. The cell geometry used in Case 1.

Compartment volume	V_{mc}	27.728 μm^3
Compartment surface	S_{mc}	9.440 μm^2
Cell membrane area	S_{ms}	5.480 μm^2
T-tubule membrane area	S_{mt}	3.960 μm^2

T-tubule, transverse tubule.

DOI: 10.1002/cnm

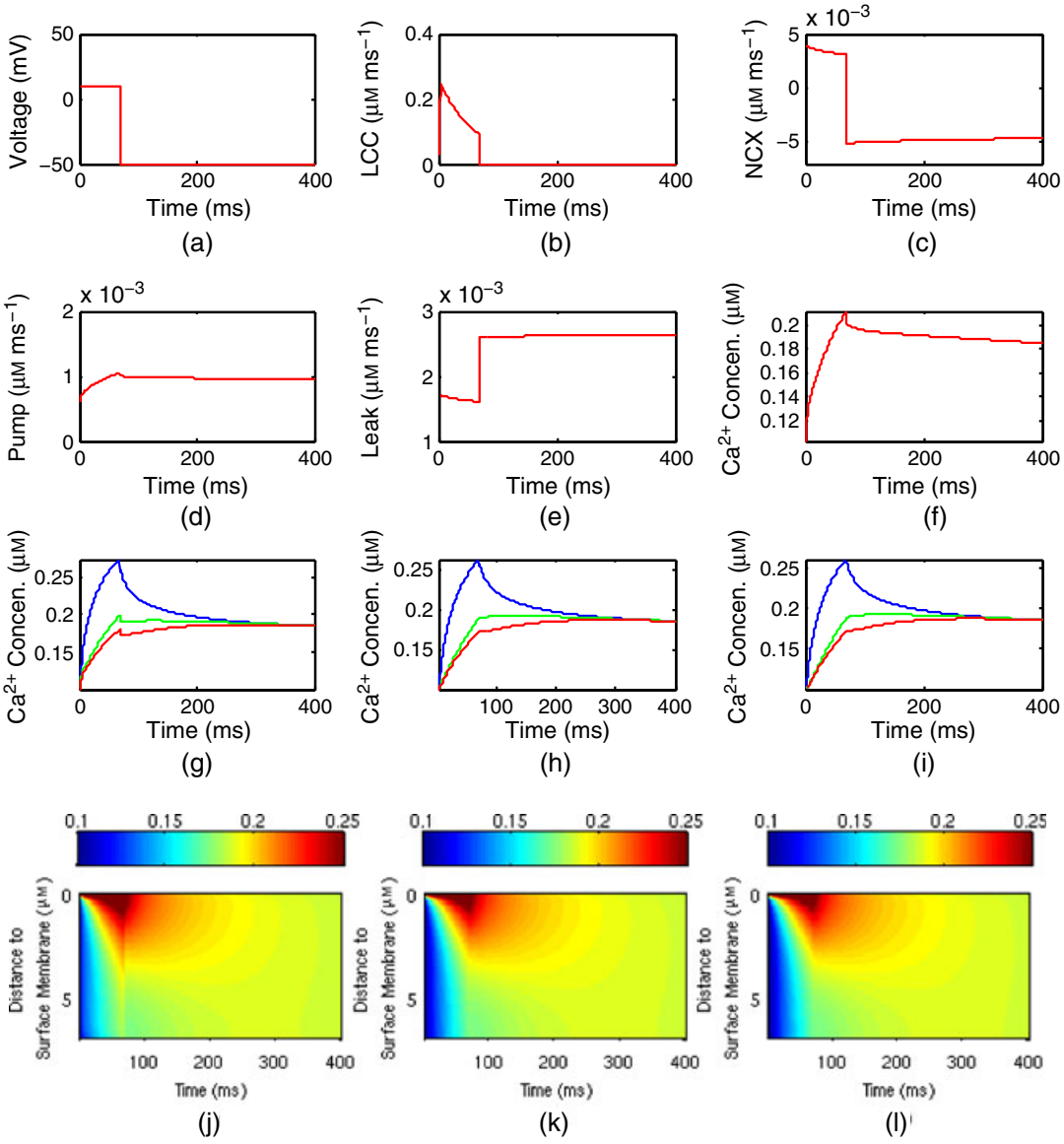

Figure 3. In this numerical experiment, the T-tubule is modeled as a cube with a dimension of 0.2 μm × 0.2 μm × 6.8 μm. (a)–(b) The voltage-clamp protocol and the whole-cell L-type calcium channel (LCC) current used in the simulation. (c)–(f) Predicted global Na^+/Ca^+, yy^{2+} pump and leak currents and global average y^{2+} transient when yyy^{2+} is uniformly distributed inside the cell. (g)–(i) Local yy^{2+} transients taken at three different line-scanned positions (the scanned line are located at (g) 0.2, (h) 0.4, and (i) 0.7 μm away from the surface of the T-tubule) and at three feature spots along the scanning line (blue, green, and red lines are 0.5, 3.6, and 7.0 μm from the cell surface, respectively). (j)–(m) Calcium concentrations visualized as line-scan images in transverse cell direction, the scanned line locations are the same as that in (g)–(i). NCX, sodium–calcium exchanger.

states, respectively. In Figure 4(h) and (i), the second picture shows a cross-section view along the T-tubule.

To investigate how the thickness of the T-tubule may affect calcium signaling, we consider the T-tubule as a line (zero thickness) instead of a cube while keeping the length unchanged. However, we assume the same cell volume, cell surface areas, and T-tubule surface area as used in Table II. The detailed transformations from the current densities to the total Ca^{2+} flux throughout the T-tubule and surface membrane are also the same as above. With all these assumptions, the predicted global

DOI: 10.1002/cnm

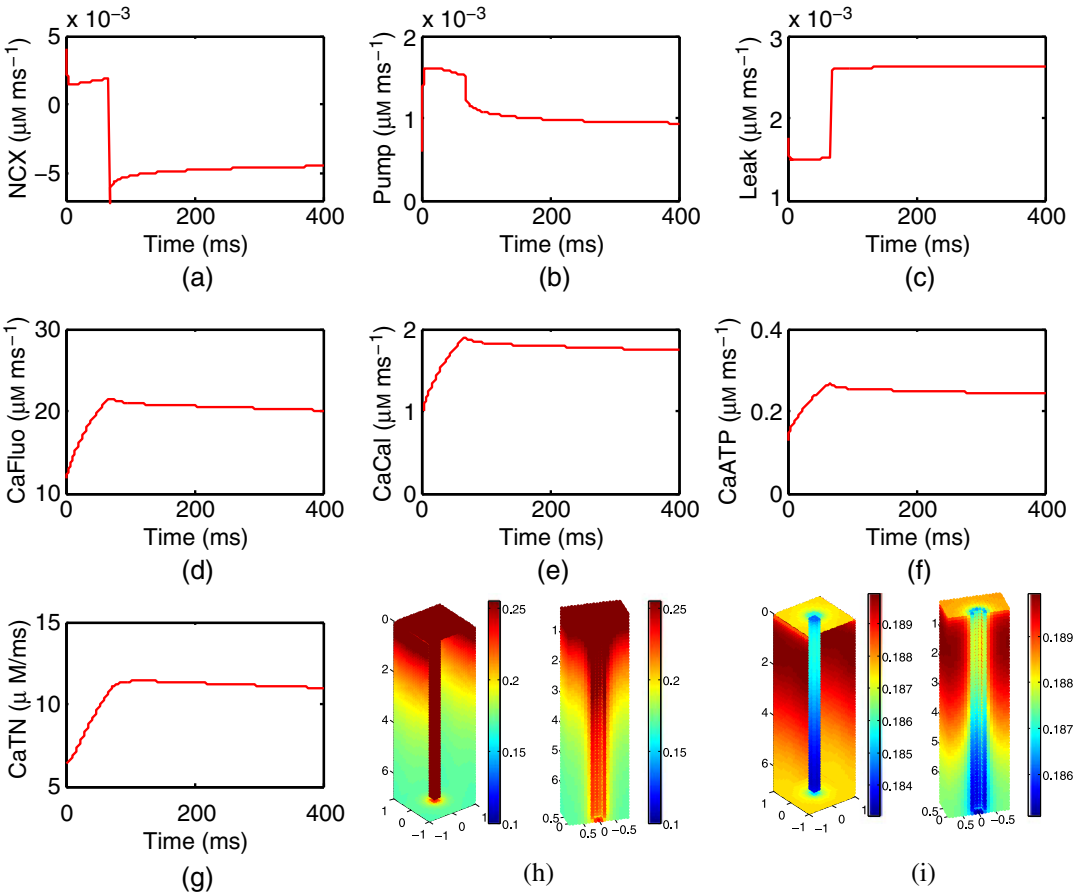

Figure 4. (a)–(c) The average Na^+/yyy^+, yy^{2+} pump and leak current densities are also predicted by using the local y^{2+} concentrations near the calcium channels. (d)–(g) Predicted average concentrations of mobile and stationary buffers over time. (h)–(i) Predicted 3D spatial yy^{2+} concentrations at 68 and 300 ms, corresponding to the yyy^{2+} peak and stable states, respectively. In (h) and (i), the second picture shows a cross-section view along the transverse tubule. NCX, sodium–calcium exchanger.

Na^+/Ca^+, Ca^{2+} pump and leak current transients are very similar to those in Figure 3. In particular, Figure 5(a) shows the predicted average Ca^{2+} concentration, which is very close to the result when the T-tubule is modeled as a cube. Figure 5(b)–(c) show the 3D local Ca^{2+} transients when $t = 68$ ms and $t = 300$ ms. Figure 5(d)–(i) shows the predicted time course Ca^{2+} transients at three scanned lines and three feature spots (the locations are the same as in Figure 3). The Ca^{2+} concentrations near the cell surface are slightly higher (see Figure 5(d)–(f)). This experiment shows that, although real T-tubules have certain thickness, treating them as line (or curve) structures can simplify mathematical simulations with comparable numerical accuracy.

6.2. *Case 2: a whole-cell model*

Consider a T-tubule-free whole-cell model described in Equation (14). The nodes in the cell are uniformly generated, where the grid distance is approximately 2 μm. The total yy^{2+} flux is

$$J_i = \beta \frac{V_{\text{mc}}}{S_{\text{mc}}} \left(\frac{1}{2\text{F}} \frac{C_m}{V_{\text{cell}}} \right) \left(I_y + I_{\text{NCX}} - I_{\text{pCa}} + I_{\text{Cab}} \right), \tag{50}$$

where the cell geometry is listed in Table III and the scaling parameter β is chosen as 25.669.

As shown in Figure 6, our model is still able to predict a high gradient near boundary regions. Figure 6(a)–(b) shows the voltage-clamp protocol and the whole-cell LCC yyy^{2+} current used

DOI: 10.1002/cnm

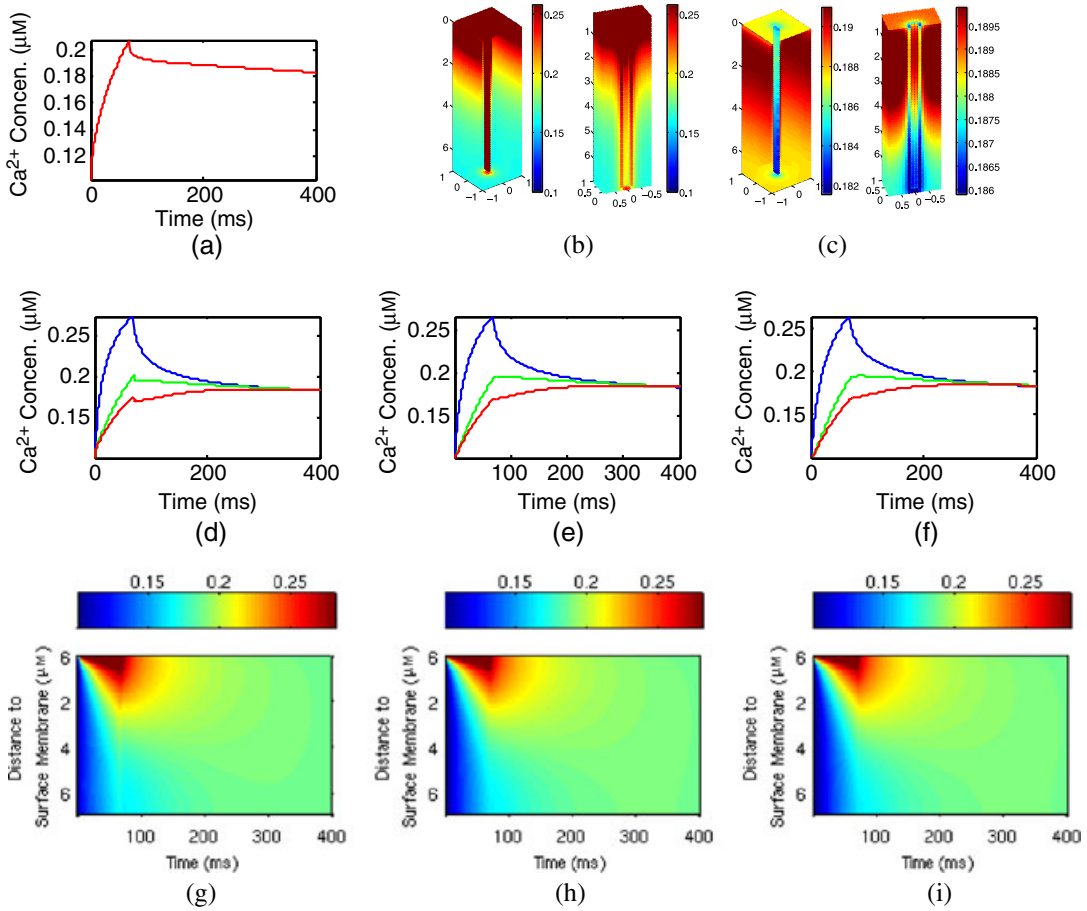

Figure 5. In this numerical experiment, the T-tubule is modeled as a single line. (a) Predict global average yy^{2+} transient when y^{2+} is uniformly distributed inside the cell. (b)–(c) Predicted 3D yy^{2+} concentration at 68 and 300 ms, respectively. (d)–(f) Local yyy^{2+} transients taken at three different line-scanned positions (the scanned line were located at (d) 0.2, (e) 0.4, and (f) 0.7 μm away from the T-tubule) and at three feature spots (blue, green, and red lines are 0.5, 3.6, and 7.0 μm from the cell surface, respectively). (g)–(i) Calcium concentrations visualized as line-scanned images in transverse cell direction, the locations of the scanned lines correspond to the cases in (d)–(f), respectively.

Table III. The cell geometry used in Case 2.

Compartment volume	V_{mc}	28237.526 μm^3
Compartment surface	S_{mc}	7713.986 μm^2

in the simulation. Figure 6(c)–(e) shows predicted Na^+/Ca^+, Ca^{2+} pump and leak when Ca^{2+} is uniformly distributed inside the cell. Figure 6(f)–(j) gives the average transients of Ca^{2+}, CaFluo, CaCal, CaATP, and CaTN. Figure 6(k)–(n) represent Ca^{2+} concentration at five feature spots along two scanned lines in transverse and longitudinal directions of the cell. Our study indicates that without T-tubular system, the Ca^{2+} signaling in ventricular myocytes is characterized by high gradients near the cell membrane.

6.3. *Discussions*

In this subsection, we discuss two issues regarding the sensitivity of the described meshless method to the shape parameter c and the number of nodes used. We first test the sensitivity to the shape parameter using the single T-tubule model (on the left of Figure 1). Figure 7 shows the predicted

DOI: 10.1002/cnm

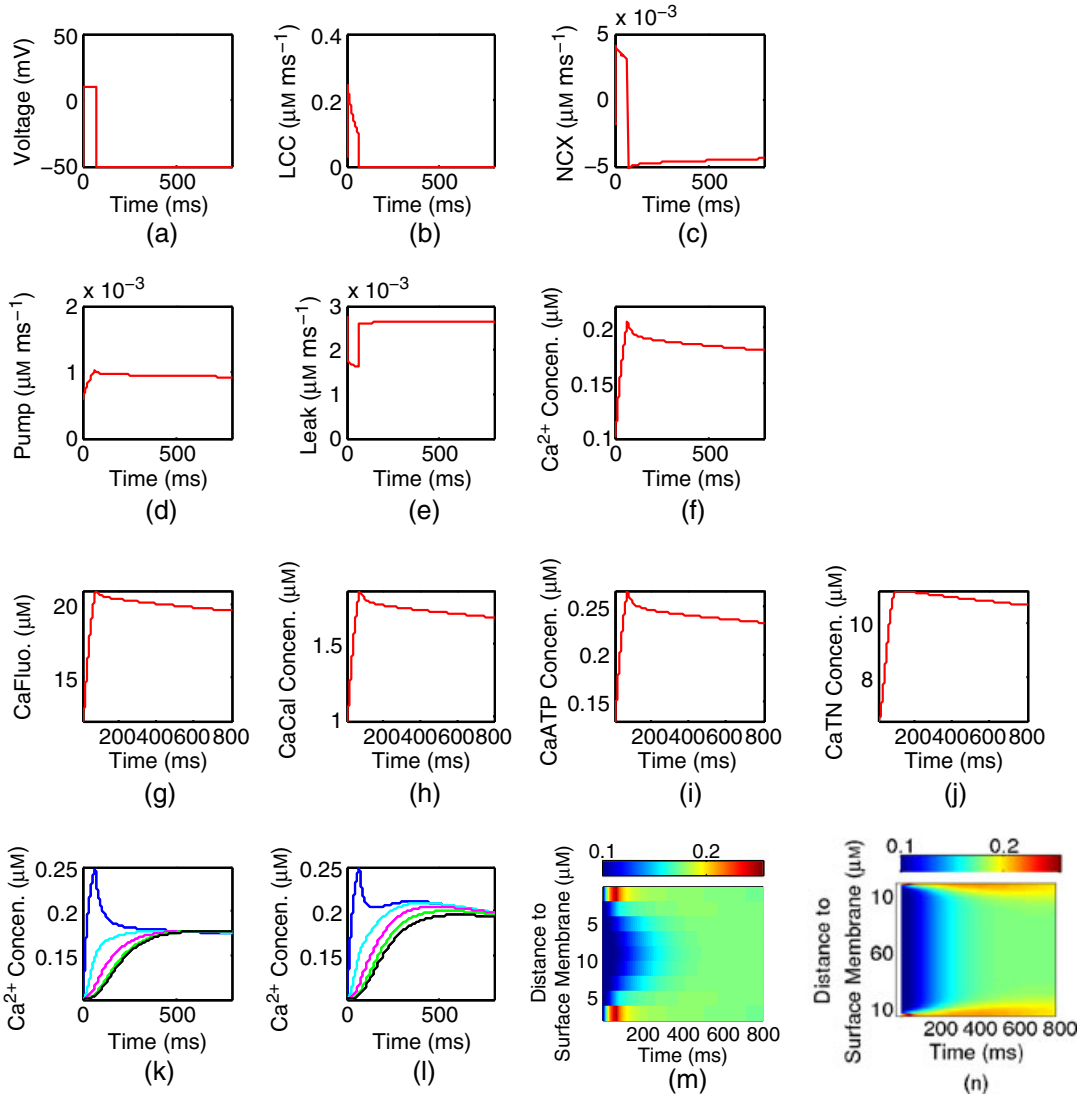

Figure 6. In this numerical experiment, L-type Ca^{2+} current density, Na^{+}/Ca^{+}, and Ca^{2+} pump were uniformly distributed on the surface of the cell. (a)–(b) The voltage-clamp protocol and the whole-cell L-type Ca^{2+} current used in the simulation. (c)–(f) Predicted global Na^{+}/Ca^{+}, Ca^{2+} pump and leak currents and global average Ca^{2+} transient when Ca^{2+} is uniformly distributed inside the cell. (g)–(j) Predicted global mobile and stationary buffer transient. (k) Local $Ca^{2}+$ transients taken at five feature spots (blue, magenta, cyan, green, and black lines are 2, 4, 6, 8, and 10 μm away from the cell membrane, respectively) along the scanning line that goes through the center of the cell in the transverse direction. (l) Local $Ca^{2}+$ transients taken at five feature spots (blue, magenta, cyan, green, and black lines are 2, 6, 12, 18, and 58 μm away from the cell membrane, respectively) along the scanning line that goes through the center of the cell in the longitudinal direction. (m)–(n) Calcium concentrations visualized as line-scan images, where the scanned lines are the same as in (k) and (l), respectively. LCC, L-type calcium channel; NCX, sodium–calcium exchanger.

time course average $[Ca^{2+}]_i$ concentration with different shape parameters, $c = 10$, 100, and 300, in which 24 297 interior points and 6510 boundary points are used. When $c = 10$, the concentration is slightly smaller than the other two cases. However, when c becomes larger, the calcium concentration remains the same. For this reason, we have used $c = 300$ in all the experiments shown earlier.

We then test the sensitivity of the meshless method to the number of nodes by using the whole-cell model (on the right of Figure 1). Figure 8 shows the predicted time course average $[Ca^{2+}]_i$

DOI: 10.1002/cnm

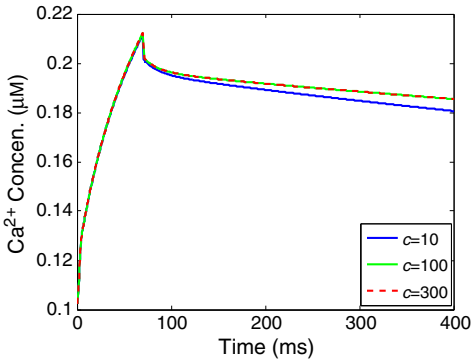

Figure 7. Predicted average $[Ca^{2+}]_i$ concentration as a function of time when different shape parameters in multiquadrics are used. In all three cases, there are 24 297 interior points and 6510 boundary points in the domain.

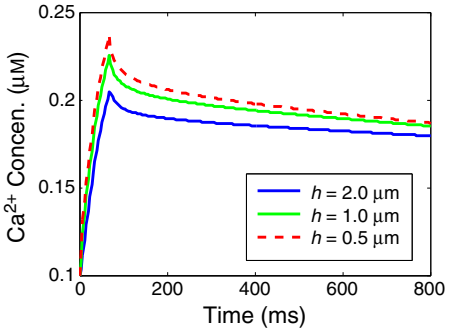

Figure 8. Predicted average $[Ca^{2+}]_i$ concentration as a function of time when different numbers of collocation points are used. Three minimum grid distances, $h = 2\mu m, 1\mu m$, and $0.5\mu m$, are considered. The corresponding numbers of nodes used are 7065, 52725, and 403, 845, respectively.

concentration with different numbers of nodes (or equivalently, grid distances h). The time-step size $\Delta t = 0.004$ ms in all cases as it meets the minimum criteria of Equation (44). The shape parameter c is chosen as 300. When the grid distance becomes two times smaller (say, h goes from 2 μm to 1 μm), the corresponding J_{Caflux} in Equation (50) at each node should be doubled accordingly (by increasing the parameter β). The reason is that the total fluxes of the model are independent of the number of nodes chosen. When the grid distance becomes two times smaller, the number of boundary nodes is expected to increase by four times, meaning that each boundary node is carrying four times fewer calcium fluxes. However, the corresponding volume of each boundary node is reduced by eight times, yielding a doubled local calcium concentration around each boundary node.

7. CONCLUSION AND FUTURE WORK

In this paper, we apply the localized meshless method called LRBFCM to solve a nonlinear system of reaction–diffusion equations in order to model Ca^{2+} dynamics in ventricular myocytes. The numerical results are compared with those in [30] to validate the proposed approaches. In contrast to the previous work [30, 48], where coupled PDEs were traditionally solved by using the FEM or the FDM, the LRBFCM does not require mesh generation that is often tedious and sometimes very difficult. Additionally, our method is flexible enough to handle complex geometric domains with competitive accuracy and low time consumption.

However, the explicit time-stepping method has a very strict constraint on time step. To avoid using impractically small time step to obtain the stable result, an implicit scheme can be considered. Implicit time-stepping methods transform time-dependent problems into a series of Helmholtz or modified Helmholtz equations. Although these methods are numerically harder to implement, we

DOI: 10.1002/cnm

could save significant computational time using these methods due to much larger time steps. Our ongoing research is focused on the utilization of implicit methods to model spatial–temporal calcium dynamics in ventricular myocytes. We shall also integrate realistic ultra-structures of T-tubules and SR from 3D imaging data into our models and investigate how SR releasing and uptaking channels affect calcium signaling.

ACKNOWLEDGEMENTS

The work described was supported in part by an NIH award (no. R15HL103497) from the National Heart, Lung, and Blood Institute (NHLBI), and by a subcontract from the National Biomedical Computation Resource (NIH award no. P41 RR08605). The content is solely the responsibility of the authors and does not necessarily represent the official views of the sponsors.

REFERENCES

1. Bers DM. Calcium cycling and signaling in cardiac myocytes. *Annual Review of Physiology* 2008; **70**:23–49.
2. Koh X, Srinivasan B, Ching HS, Levchenko A. A 3D Monte Carlo analysis of the role of dyadic space geometry in spark generation. *Biophysical Journal* 2006; **90**(6):1999–2014.
3. Izu LT, Means SA, Shadid JN, Chen-Izu Y, Balke CW. Interplay of ryanodine receptor distribution and calcium dynamics. *Biophysical Journal* 2006; **91**(1):95–112.
4. Bers DM. Cardiac excitation–contraction coupling. *Nature* 2002; **415**(6868):198–205.
5. Wu L, Kwok Y. A front-fixing finite difference method for the valuation of American options. *Journal of Financial Engineering* 1997; **6**(2):83–97.
6. Braess D. *Finite Elements: Theory, Fast Solvers and Applications in Solid Mechanics*. Cambridge University Press, 2001.
7. Melenk J, Babuška I. The partition of unity finite element method: basic theory and applications. *Computer Methods in Applied Mechanics and Engineering* 1996; **139**(4):289–314.
8. Eymard R, Gallouet T, Herbin R. Finite volume methods, *Techniques of Scientific Computing, Vol VII*, Ciarlet PG, Lions JL (eds): North-Holland, 2000; 713–1020.
9. Schaback R. Convergence analysis of methods for solving general equations, *Boundary Elements XXVII*, Kassab A, Brebbia CA, Divo E, Poljak D (eds). WITPress: Southampton, 2005; 17–24.
10. Schaback R, Wendland H. Using compactly supported radial basis functions to solve partial differential equations, *Boundary Element Technology XIII*, Chen CS, Brebbia CA, Pepper D (eds). WITPress: Southampton, 1999; 311–324.
11. Golberg MA, Chen CS, Karur SR. Improved multiquadric approximation for partial differential equations. *Engineering Analysis with Boundary Elements* 1996; **18**:9–17.
12. Atluri SN, Shen S. *The Meshless Local Petrov–Galerkin (MLPG) Method*. Tech Science Press: Encino, CA, 2002.
13. Liu GR. *Mesh Free Methods: Moving Beyond the Finite Element Method*. CRC Press: Boca Raton, FL, 2002.
14. Mai-Duy N, Tran-Cong T. Mesh-free radial basis function network methods with domain decomposition for approximation of functions and numerical solution of Poisson's equation. *Engineering Analysis with Boundary Elements* 2002; **26**(2):133–156.
15. Fasshauer GE. *Meshfree Approximation Methods with MATLAB*. World Scientific Press: Singapore, 2007.
16. Atluri SN. *The Meshless Method MLPG for Domain and BIE, Discretizaion*. Tech. Sci. Press: USA, 2004.
17. Liu GR, Dai KY, Lim KM, Gu YT. A point interpolation meshfree method for static and frequency analysis of two-dimensional piezoelectric structures. *Computational Mechanics* 2002; **29**(6):510–519.
18. Chen W. New RBF collocation schemes and kernel RBFs with applications. *Lecture Notes in Computational Science and Engineering* 2002; **26**:75–86.
19. Wen PH, Chen CS. The method of particular solutions for solving scalar wave equations. *International Journal for Numerical Methods in Biomedical Engineering* 2010; **26**(12):1878–1889.
20. Karageorghis A, Chen CS, Smyrlis YS. Matrix decomposition RBF, algorithm for solving 3D elliptic problems. *Engineering Analysis with Boundary Elements* 2009; **33**(12):1368–1373.
21. Lee CK, Liu X, Fan SC. Local multiquadric approximation for solving boundary value problems. *Computational Mechanics* 2003; **30**:396–409.
22. Shu C, Ding H, Yeo KS. Local radial basis function-based differential quadrature method and its application to solve two dimensional incompressible navier-stokes equations. *Computer Methods in Applied Mechanics and Engineering* 2003; **192**(7–8):941–954.
23. Šarler B, Vertnik R. Meshfree explicit local radial basis function collocation method for diffusion problems. *Computers and Mathematics with Applications* 2006; **51**(8):1269–1282.
24. Vertnik R, Šarler B. Meshless local radial basis function collocation method for convective–diffusive solid–liquid phase change problems. *International Journal of Numerical Methods for Heat and Fluid Flow* 2006; **16**(5):617–640.
25. Vertnik R, Zaloznik M, Šarler B. Solution of transient direct-chill aluminum billet casting problem with simultaneous material and interphase moving boundaries by a meshless method. *Engineering Analysis with Boundary Elements* 2006; **30**(10):847–855.

DOI: 10.1002/cnm

26. Kovacevic I, Šarler B. Solution of a phase-field model for dissolution of primary particles in binary aluminum alloys by an r-adaptive mesh-free method. *Material Science and Engineering A* 2005; **413/414**:423–428.
27. Divo E, Kassab AJ. An efficient localized RBF meshless method for fluid flow and conjugate hear transfer. *ASME Journal of Heat Transfer* 2007; **129**:124–136.
28. Kosec G, Šarler B. Local RBF collocation method for darcy flow. *Computer Modeling in Engineering and Sciences* 2008; **25**(3):197–208.
29. Vertnik R, Šarler B. Solution of incompressible turbulent flow by a mesh-free method. *Computer Modeling in Engineering and Sciences* 2009; **44**(1):65–95.
30. Lu S, Michailova A, Saucerman J, Cheng Y, Yu Z, Bank R, Kaiser T, Li W, Holst M, McCammon J, Hayashi T, Arzberger P, McCulloch A, Cheng Y, Hoshijima M. Multiscale modeling in rodent ventricular myocytes. *Engineering in Medicine and Biology Magazine, IEEE* 2009; **28**:46–57.
31. Matveev V, Zucker RS, Sherman A. Facilitation through buffer saturation: constraints on endogenous buffering properties. *Biophysical Journal* 2004; **86**(5):2691–2709.
32. Zahradnikova A, Kubalova Z, Pavelkova J, Gyorke S, Zahradnik I. Activation of calcium release assessed by calcium release-induced inactivation of calcium current in rat cardiac myocytes. *American J. of Physiology* 2004; **286**(2):C330–C379.
33. Hinch R, Greenstein JL, Tanskanen AJ, Xu L, Winslow R. A simplified local control model of calcium-induced calcium release in cardiac ventricular myocytes. *Biophysical Journal* 2004; **87**(6):3723–3736.
34. Soeller C, Cannell MB. Examination of the transverse tubular system in living cardiac rat myocytes by 2-photon microscopy and digital image processing techniques. *Circulation Research* 1999; **84**(3):266–275.
35. Michailova A, DelPrincipe F, Egger M, Niggli E. Spatiotemporal features of Ca2+ buffering and diffusion in atrial cardiac myocytes with inhibited sarcoplasmic reticulum. *Biophysical J.* 2002; **83**(6):3134–3151.
36. Satoh H, Delbridge LM, Blatter LA, Bers DM. Surface: Volume relationship in cardiac myocytes studied with confocal microscopy and membrane capacitance measurements: species-dependence and developmental effects. *Biophysical J.* 1996; **70**(3):1494–1504.
37. Pasek M, Brette F, Nelson A, Pearce C, Qaiser A, Orchard C, Christe G. Quantification of T-tubule area and protein distribution in rat cardiac ventricular myocytes. *Progress in Biophysics and Molecular Biology* 2008; **96**(1–3):244–257.
38. Balakrishnan K, Sureshkumar R, Ramachandran PA. An operator splitting-RBF method for the solution of transient nonlinear Poisson problems. *Computers and Mathematics with Applications* 2002; **43**(3–5):289–304.
39. Micchelli CA. Interpolation of scattered data: distance matrix and conditionally positive definite functions. *Constr. Approx.* 1986; **2**:11–22.
40. Wang JG, Liu GR. On the optimal shape parameters of radial basis functions used for 2-D meshless methods. *Computer Methods in Applied Mechanics and Engineering* 2002; **191**:2611–2630.
41. Wertz Z, Kansa EJ, Ling L. The role of the multiquadric shape parameters in solving elliptic partial differential equations. *Computer and Mathematics with Applications* 2006; **51**(8):1335–1348.
42. Bentley JL. Multidimensional divide-and-conquer. *Communications of the ACM* 1980; **23**(4):214–229.
43. Friedman JH, Bentley JL, Finkel RA. An algorithm for finding best matches in logarithmic expected time. *ACM Trans. on Mathematical Software* 1977; **3**(3):209–226.
44. Guttman A. R-trees: A dynamic index structure for spatial searching. *Proceedings of the International Conference of Management of Data (ACM SIGMOD)*. ACM: New York Press, 1984; 47–57.
45. Indyk P, Motwani R. Approximate nearest neighbors: Towards removing the curse of dimensionality. *Proceedings of the 30th Annual ACM Symposium on Theory of Computing*, 1998; 604–613.
46. Omohundro SM. Efficient algorithms with neural network behavior. *Complex Systems* 1987; **1**:273–347.
47. Courant R, Friedrichs K, Lewy H. On the partial difference equations of mathematical physics. *IBM J. Res. Dev* 1967; **11**(2):215–234.
48. Tewari S, Pardasani K. Finite difference model to study the effects of Na^+ influx on cytosolic Ca^{2+} diffusion. *International Journal of Biological and Life Sciences* 2008; **4**(4):205–210.

DOI: 10.1002/cnm